

Effect of TiB₂ Nanoparticles on Microstructure and Mechanical Properties of Ni₆₀Cr₂₁Fe₁₉ Alloy in Rapid Directional Solidification Process: Molecular Dynamics Study

WANG Jin, JIANG Wugui*, HU Chenxi

School of Materials Science and Engineering, Nanchang Hangkong University, Nanchang 330063, P. R. China

(Received 4 June 2024; revised 10 August 2024; accepted 15 October 2024)

Abstract: Molecular dynamics (MD) simulations are employed to delve into the multifaceted effects of TiB₂ nanoparticles on the intricate grain refinement mechanism, microstructural evolution, and tensile performance of Inconel 718 superalloys during the rapid directional solidification. Specifically, the study focuses on elucidating the role of TiB₂ nanoparticles in augmenting the nucleation rate during the rapid directional solidification process of Ni₆₀Cr₂₁Fe₁₉ alloy system. Furthermore, subsequent tensile simulations are conducted to comprehensively evaluate the anisotropic behavior of tensile properties within the solidified microstructures. The MD results reveal that the incorporation of TiB₂ nanoparticles during the rapid directional solidification of the Ni₆₀Cr₂₁Fe₁₉ significantly enhances the average nucleation rate, escalating it from $1.27 \times 10^{34} \text{ m}^{-3} \cdot \text{s}^{-1}$ to $2.55 \times 10^{34} \text{ m}^{-3} \cdot \text{s}^{-1}$. Notably, within the face centered cube (FCC) structure, Ni atoms exhibit pronounced compositional segregation, and the solidified alloy maintains an exceptionally high dislocation density reaching up to 10^{16} m^{-2} . Crucially, the rapid directional solidification process imparts a distinct microstructural anisotropy, leading to a notable disparity in tensile strength. Specifically, the tensile strength along the solidification direction is markedly superior to that perpendicular to it. This disparity arises from different deformation mechanisms under varying loading orientations. Tensile stress perpendicular to the solidification direction encourages the formation of smooth and organized mechanical twins. These twins act as slip planes, enhancing dislocation mobility and thereby improving stress relaxation and dispersion. Moreover, the results underscore the profound strengthening effect of TiB₂ nanoparticles, particularly in enhancing the tensile strength along the rapid directional solidification direction.

Key words: TiB₂ nanoparticle; rapid directional solidification; microstructure evolution; molecular dynamics

CLC number: TB31

Document code: A

Article ID: 1005-1120(2024)05-0575-14

0 Introduction

Inconel 718 (IN718) alloy, a nickel-based superalloy, is widely used in pivotal industries including aerospace, energy, chemical processing, and automotive, thanks to its exceptional mechanical properties and high-temperature stability^[1-3]. In recent years, with the rapid advancement of additive manufacturing (AM) technology, selective laser melting (SLM) has been successfully applied to the production of intricate structures utilizing IN718 alloy, marking significant progress in this domain^[4].

During the SLM process, the IN718 alloy forms unique microstructures and mechanical properties due to the high thermal gradients and rapid cooling rates, exhibiting significant advantages compared to traditional processes such as forging and casting^[5-8].

To further optimize the performance of SLM-processed IN718 alloy, researchers have discovered that the addition of specific nucleating agents can effectively refine the grain structure while maintaining the alloy's toughness, which is crucial for enhancing its mechanical properties. TiB₂ nanoparticles, as

*Corresponding author, E-mail address: jiangwugui@nchu.edu.cn.

How to cite this article: WANG Jin, JIANG Wugui, HU Chenxi. Effect of TiB₂ nanoparticles on microstructure and mechanical properties of Ni₆₀Cr₂₁Fe₁₉ alloy in rapid directional solidification process: Molecular dynamics study [J]. Transactions of Nanjing University of Aeronautics and Astronautics, 2024, 41(5): 575-588.

<http://dx.doi.org/10.16356/j.1005-1120.2024.05.003>

an efficient grain refiner, have demonstrated significant refinement effects in pure nickel^[9] and diverse alloys^[10], underscoring their potential value in alloy engineering. However, directly observing the microstructural evolution of the alloy during the solidification phase through experiments poses significant challenges, constrained not only by the complexity of experimental techniques but also by the high economic and time costs involved.

To overcome these limitations and achieve deeper understanding, researchers have turned to molecular dynamics (MD) simulations as a powerful tool. This computational methodology facilitates precise simulation of atomic-level dynamics, providing a robust and efficient framework for exploring the nucleation mechanisms underlying rapid directional solidification processes^[11-15]. For instance, Cao et al.^[14] successfully utilized MD simulations to elucidate the directional solidification behavior of Al-Si10Mg alloy during additive manufacturing processes, while Fujinaga et al.^[15] further validated the methodology by simulating the impact of Al-Ti refiners on the solidification of aluminum, reinforcing the efficacy of MD simulations in alloy modification research.

It is well-known that the intricate microstructural details formed during the solidification process are crucial in determining the tensile mechanical properties of alloys. MD simulations have emerged as a powerful tool for probing the intricate tensile behavior of diverse materials, both in directions parallel and perpendicular to the rapid directional solidification. For example, MD studies on materials such as twinning-induced plasticity (TWIP) have unveiled remarkable twinning-induced plasticity phenomena, accompanied by the manifestation of Shockley dislocations and intricate interplay between stacking faults and grain boundaries, irrespective of the applied load orientation^[16]. Analogously, high-entropy alloys, exemplified by CoCrCuFeNi, have been extensively studied using MD simulations, revealing comparable microstructural evolutions and mechanical responses during tensile examinations^[17]. These simulations have further validated the versatility and predictive capabilities of MD methods in elucidating

the intricate material behavior under various loading conditions. Similarly, Hu et al.^[18] employed MD simulations to delve into the mechanical properties and microstructural dynamics of Cu/Ta composites under uniaxial tension. Their study elucidated the profound influence of diverse interface structures on dislocation mobility, stacking fault formation, and deformation mechanisms, thereby showcasing the power of MD simulations in capturing the nuanced interplay between microstructure and mechanical behavior at the atomic scale.

To ensure the reliability of MD results, the key lies in selecting appropriate potential energy functions and ensembles, as well as setting proper boundary conditions and time steps. In this study, a classical embedded atom method (EAM) potential^[19] is adopted for Ni-Cr-Fe, while a modified embedded atom method (MEAM) potential^[20] specifically developed for this system is used for TiB. The choice of ensemble, boundary conditions, and time step settings follows similar configurations from existing work^[11-13], thereby ensuring the reliability of the MD simulation results.

In this study, Ni₆₀Cr₂₁Fe₁₉ is selected as a feasible substitute of IN718 alloy due to their similar composition. This choice is grounded on the findings of Wang et al.^[21], who discovered that the simulated density values of Ni₆₀Cr₂₁Fe₁₉ closely match those of IN718 alloy, providing a reasonable basis for utilizing MD simulations of Ni₆₀Cr₂₁Fe₁₉ to investigate the rapid directional solidification process of IN718 alloy.

The primary objective of this study is to employ MD simulations to explore the influence of TiB₂ nanoparticles on the rapid directional solidification process of IN718 alloy. By applying specific temperature gradients, the rapid solidification process of the alloy is simulated, and then subsequent tensile simulations are conducted to comprehensively evaluate the anisotropic behavior of tensile properties within the solidified microstructures. This approach aims to provide a deep understanding of how TiB₂ nanoparticles regulate the rapid directional solidification process and mechanical properties of the SLM-processed IN718 alloy, thereby offering theoretical support for the design of alloys.

1 Modeling and Methods

1.1 Rapid directional solidification model

In the context of the SLM process, rapid solidification poses a significant complexity owing to the intricate thermal dynamics within the system, as vividly depicted in Fig.1. This intricate process necessitates meticulous thermal management, encompassing precise temperature control, intricate heat transfer mechanisms, and multidimensional heat distribution. Additionally, it involves complex thermal interactions that span across different material layers and interfaces, further compounding the challenge. Acknowledging the inherent computational constraints of MD simulations, this study adopts a simplified approach to streamline the rapid solidification process in SLM process. Specifically, it focuses on the fundamental phenomenon induced by considering solely one-dimensional temperature gradients, thereby enabling an in-depth analysis within the feasible computational bounds.

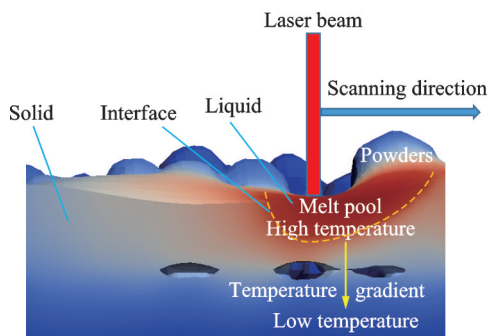


Fig.1 Schematic of rapid directional solidification in SLM

To explore the atomic-level effects of TiB₂ nanoparticles on the rapid directional solidification process of IN718 alloy, we craft a designed simulation domain, a compact cube of 10 nm × 10 nm × 10 nm, encompassing a total of 87 221 atoms, as clearly illustrated in Fig.2(a). This configuration, inclusive of a sophisticated the rapid directional solidification simulation apparatus, is necessitated by the formidable computational demands of the MEAM potential^[22]. Notably, experiments conducted by Zhao et al.^[23] revealed that TiB₂ nanoparticles at a mass percentage of 2% exhibited superior grain refinement effects in IN718 alloy during solidifica-

tion compared to those at 1%. However, their study did not conclusively determine an optimal percentage.

In this study, at the center of this computational realm, a TiB₂ nanoparticle with a radius of 1.9 nm (i.e. a mass percentage of 3%) is strategically positioned, comprising Ti and B atoms in an exact 1:2 stoichiometric ratio, occupying a substantial 3% of the overall simulation box volume. Surrounding this spherical TiB₂ nanoparticle, Ni, Cr, and Fe atoms are randomly arranged in a lattice structure, adhering to a precise 60:21:19 compositional ratio, ensuring a realistic representation of the alloy. Fig.2(b) offers a captivating cross-sectional view of the TiB₂-Ni₆₀Cr₂₁Fe₁₉ model, where the diverse atomic species are distinguished by their unique color coding: Cr atom in red, Ni atom in blue, Fe atom in yellow, Ti atom in purple, and B atom in green. Furthermore, to provide a comparative benchmark, we have also established an identical-sized simulation model, devoid of TiB₂ nanoparticles, enabling a comprehensive analysis of the nanoparticle's influence on the rapid directional solidification process.

Initially, the simulation box is heated to a temperature exceeding the melting point of IN718 (T_m) but remaining below the melting point of the TiB₂ nanoparticles (3 498 K)^[24]. This strategic approach ensures the Ni₆₀Cr₂₁Fe₁₉ alloy attains a homogeneous molten state, whereas the TiB₂ nanoparticles maintain their solid form, functioning effectively as grain refiners. Throughout this stage, the box's temperature is stabilized at 2 500 K, utilizing the NPT ensemble with a time step of 3 fs for a duration of 150 ps. The Nose-Hoover thermostat and Parrinello-Rahman barostat regulate temperature and pressure, respectively, ensuring consistent conditions. Periodic boundary conditions are imposed in all three dimensions during this preparatory stage.

Subsequently, the simulation box is precisely divided into three regions during the rapid directional solidification simulation, as illustrated in Fig.2(a). The temperature settings are based on the methodology of Bahramyan et al.^[16]. The leftmost 1 nm strip serves as the low-temperature zone, held at a con-

stant low temperature of 1 190 K ($0.7T_m$, where T_m for $\text{Ni}_{60}\text{Cr}_{21}\text{Fe}_{19}$ is 1 700 K) [25]. Conversely, the rightmost 1 nm zone acts as the high-temperature zone, maintained at a constant high temperature of 1 462 K ($0.86T_m$). The high and low-temperature regions are kept constant using a Langevin thermostat, while the intermediate zone remains uncontrolled, fostering a natural temperature gradient. During the solidification simulation, the microcanonical ensemble (NVE) is employed. Critically, the periodic boundary condition along the solidification direction is replaced with a shrink-wrapped boundary condition, enhancing the realism of the simulation. Over a period of 5 ns, simulations are conducted within the specified temperature range ($0.7T_m$ to $0.86T_m$), with the time step refined to 1 fs to meticulously track every nuance of the rapid directional solidification process.

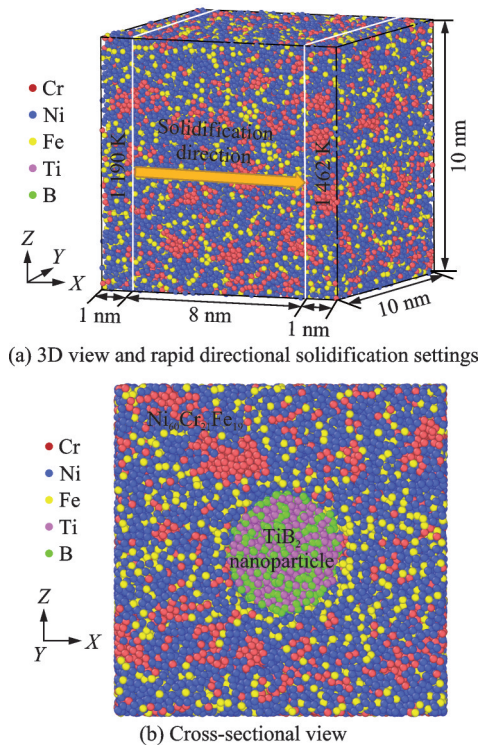


Fig.2 Initial configuration of $\text{TiB}_2\text{-Ni}_{60}\text{Cr}_{21}\text{Fe}_{19}$

1.2 Tensile model

After the completion of the solidification process simulation, to ensure the accuracy of the tensile simulation, the outer 1-nm-wide regions at ambient temperature from the model are removed. This reduction led to a further shrinkage of the mod-

el size to $8\text{ nm} \times 8\text{ nm} \times 8\text{ nm}$. It is noteworthy that such a small atomic model struggles to encompass an adequate number of grains, potentially compromising the representativeness and accuracy of the tensile simulation results.

To preliminarily assess the potential impact of TiB_2 on tensile properties, Fig.3 depicts the tensile stress-strain curves for two different sizes of $\text{Ni}_{60}\text{Cr}_{21}\text{Fe}_{19}$ alloy models: 8 nm (with and without TiB_2 nucleating agents) and 16 nm (without TiB_2 nucleating agents). The results indicate that for the 8 nm model, regardless of the presence of TiB_2 nucleating agents, the tensile properties exhibit weak anisotropy. Compared to the model without TiB_2 , the model with added TiB_2 nucleating agents shows slightly higher tensile stress in both the X and Z directions, albeit the difference is not pronounced. In contrast, for the larger 16 nm model without TiB_2 nucleating agents, the tensile stress demonstrates stronger anisotropy, particularly with significantly higher stress along the X -direction compared to the Z -direction.

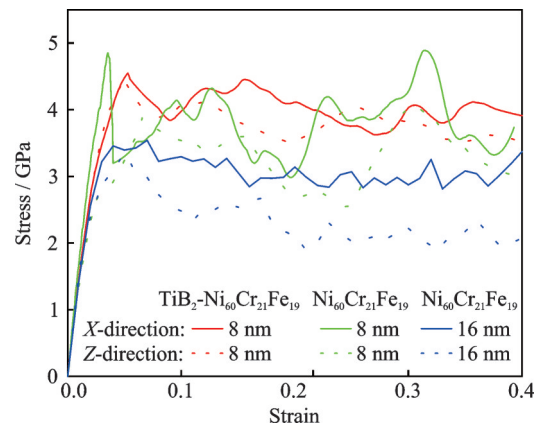


Fig.3 Tensile stress-strain curves for two different sizes of models

Given the current unavailability of a suitable EAM potential tailored for TiB_2 systems and the substantial limitations of the MEAM potential in handling large-scale computations [26], the MD simulations for larger 16 nm model with TiB_2 nucleating agents are not conducted here.

Constructing a sufficiently large atomic model to directly simulate the specific mechanisms of TiB_2

nanoparticles during tensile processes is crucial for a comprehensive understanding of material strengthening mechanisms. However, under current technological conditions, achieving this goal poses numerous challenges, including significant increases in computational complexity and time costs. Therefore, in this paper, we have focused on exploring the promotional effect of TiB₂ nanoparticles on grain refinement during the solidification stage and discussing how this refinement effect indirectly enhances the mechanical properties of materials through microstructural improvements.

The atomic models for tensile simulations are constructed by relying on the grain statistical analysis within the solidified microstructures. Utilizing the grain segmentation method, a polyhedral template matching (PTM) analysis is conducted on the solidified atomic configurations to characterize their structural features. By calculating the total number of grains and the ratio of this number to the overall volume, the average grain volume is determined. Subsequently, this average grain volume is equated to a spherical model, enabling the calculation of the average grain diameter. After rapid directional solidification, the Ni₆₀Cr₂₁Fe₁₉ model reveals an average grain diameter of 8.22 nm, whereas the incorporation of TiB₂ in the Ni₆₀Cr₂₁Fe₁₉ model results in a refined average grain diameter of 7.1 nm, highlighting the grain-refining effect of TiB₂ nanoparticles.

Inspired by the experimental findings of Kurdi et al.^[27], a pronounced dichotomy was discerned in the SLM-processed IN718 alloy: The low-temperature zone exhibited a gradual progression towards a columnar grain structure, whereas the high-temperature region showcased a uniformly dispersed equiaxed grain arrangement, embodying the hybrid grain architectures frequently encountered in additive manufacturing processes. Consequently, the dimensions of the tensile model are meticulously designed to encompass approximately 30 nm × 15 nm × 15 nm, accommodating approximately 620 798 atoms.

As depicted in Fig.4, the simulation box is divided into two distinct regions: Region One contains either five or four columnar grains, each with a

cross-sectional diameter of 7.1 nm or 8.2 nm and a length of 20 nm. Region Two encompasses 12 or 10 equiaxed grains, modeled as spheres of equivalent diameter, corresponding to the TiB₂-Ni₆₀Cr₂₀Fe₁₉ (Fig.4(a)) and Ni₆₀Cr₂₀Fe₁₉ (Fig.4(b)) tensile models, respectively. This partition aims to analyze the changes in mechanical properties resulting from grain refinement in Ni₆₀Cr₂₀Fe₁₉ after the introduction of TiB₂ as a nucleating agent.

Furthermore, recognizing the prevalence of thermally induced twins (TTs) in the solidified microstructure, the tensile model is initially endowed with twins, mirroring these thermally generated features. Fig.4 vividly illustrates this constructed tensile model, where red highlights the thermal twins formed during the rapid directional solidification process, white demarcates grain boundaries (GBs), and green represents the face centered cube (FCC) structure.

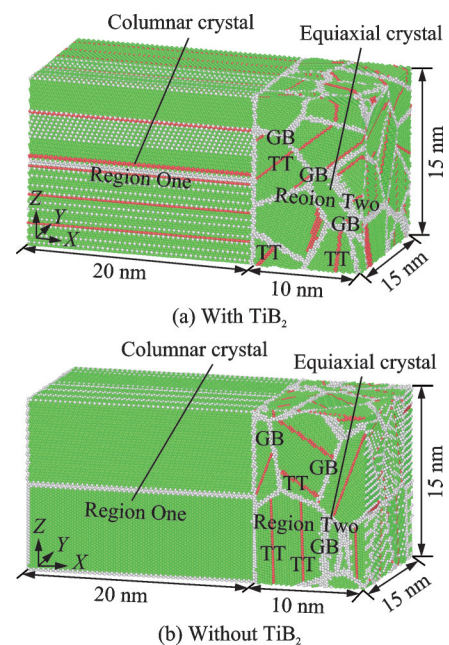


Fig.4 Atomic configuration under tensile load for Ni₆₀Cr₂₁Fe₁₉

Fig.5 provides a comprehensive overview of the distribution of equiaxed and columnar grains within the simulation box for the TiB₂-Ni₆₀Cr₂₀Fe₁₉ tensile model, elucidating their number and volume size contributions.

To evaluate the tensile properties of the final solidified Ni₆₀Cr₂₁Fe₁₉ structure, simulations are per-

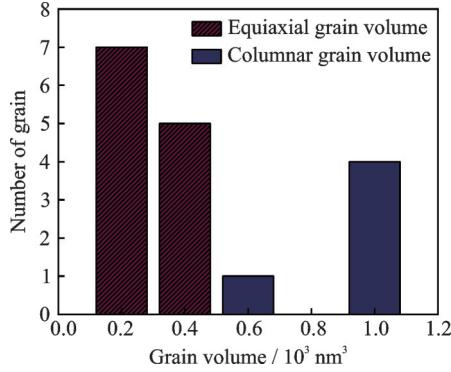


Fig.5 Number and volume size distribution of equiaxial and columnar grains

formed under the NPT ensemble at 300 K, applying a strain rate of $5 \times 10^8 \text{ s}^{-1}$ along both the X -axis (solidification direction) and the Z -axis (perpendicular to the solidification direction) for a duration of 1 ns, with a time step of 1 fs, ensuring precision and accuracy in capturing the material's dynamic response.

1.3 Atomic potentials

In MD simulations, the choice of potential functions holds paramount importance, directly influencing the accuracy and reliability of the results. This study leverages three specific potentials: EAM, MEAM, and Lennard-Jones (L-J) potential.

For the Ni-Cr-Fe system, the study adopts the EAM potential formulated by Mendelev^[19], which is expressed as

$$E_{\text{total}} = \sum_i \left[\frac{1}{2} \sum_j \Phi(r_{ij}) + F(\rho_i) \right] \quad (1)$$

where r_{ij} represent the distances between atoms i and j ; $\Phi(r_{ij})$ the traditional pair potential functions; ρ_i the electron cloud density at atom i ; and $F(\rho_i)$ the embedding energy of an atom as a function of the electron cloud density ρ_i .

To extend the applicability of the EAM potential to a broader range of materials, including metals, semiconductors, and even diatomic gases, Baskes proposed the more versatile MEAM model in 1992^[28]. This model not only maintains the efficiency and intuitiveness of EAM but also incorporates enhancements that significantly bolster its ability to handle intricate many-body interactions.

In the context of rapid directional solidification simulations, the MEAM potential tailored by Attarian and Xiao for the TiB system^[20] is employed. Analogous to Eq.(1), the total energy in the MEAM model is approximated as the cumulative energies of all atoms within the system

$$E_{\text{total}} = \sum_i \left[\sum_j F(\bar{\rho}_i) + \frac{1}{2} \sum_j \Phi(r_{ij}) \cdot S_{ij} \right] \quad (2)$$

In this model, the energy of atom i composes of the embedding energy, interaction energy, and the screening function S_{ij} . Notably, the MEAM model incorporates angular-dependent terms to refine the electron density $\bar{\rho}_i$, significantly enhancing its capability to capture the complex internal electronic structures of materials, surpassing the simple electron density descriptions in traditional EAM models.

Additionally, the L-J potential^[29] is utilized to describe the non-bonded interactions between the element pairs Ni-Ti, Ni-B, Cr-Ti, Cr-B, Fe-Ti, and Fe-B, which is expressed as

$$U(r_{ij}) = 4\epsilon \left[\left(\frac{\sigma}{r_{ij}} \right)^{12} - \left(\frac{\sigma}{r_{ij}} \right)^6 \right] \quad (3)$$

where $U(r_{ij})$ is the intermolecular potential between two atoms or molecules; ϵ is the depth of the potential well, which measures the strength of the attraction between the two particles; σ is the distance at which the intermolecular potential is zero; r is the distance of separation between both particles; The first half of the equation, $(\sigma/r_{ij})^{12}$ describes the repulsive forces, while the second half, $(\sigma/r_{ij})^6$ describes the attractive forces.

In this study, the foundational atomic models for both rapid directional solidification and tensile testing scenarios are meticulously crafted utilizing the ATOMSK software package^[30]. Subsequently, the LAMMPS simulation code^[31] serves as the backbone for simulating the intricate process of rapid directional solidification of TiB₂ nanoparticles embedded within the IN718, alongside the subsequent tensile deformation process. For a comprehensive understanding and analysis of these simulations, the OVITO software^[32] is employed, facilitating insightful visualization and rigorous data interpretation.

2 Results and Discussion

2.1 Evolution of crystal structure during rapid directional solidification

Fig.6 illustrates the intricate process of crystal growth during rapid directional solidification, where atoms are color-coded through common neighbor analysis (CNA)^[33], enabling a vivid visualization of the transformation in atomic structure types throughout the solidification phase. Atoms with FCC structures are colored in green, hexagonal close-packed (HCP) structures in red, body-centered cubic (BCC) structures in blue, and liquid or amorphous atoms in white.

At 1.8 ns, the nucleation of crystals can be distinctly observed in the low-temperature region, marking the onset of the heterogeneous solidification. By 2 ns, these nascent nuclei proliferate and gradually mature into small grains, upon whose surfaces new nuclei subsequently emerge. At 2.2 ns, the solidified crystals advance steadily from the cooler left side towards the warmer right region. By 2.4 ns, the rapid directional solidification process is nears completion, with the solidified microstructure predominantly exhibiting the characteristic FCC structure, complemented by thermally induced HCP twins (TTs) with diverse grain orientations, prominently visible in Fig.6. Additionally, as shown in Fig.6, a PTM polycrystalline analysis is conducted using a particle tracking methodology, where grains comprising over 1 000 atoms are uniquely color-coded, and each hue representing a distinct grain. Grains with fewer than 1 000 atoms are rendered white to ensure a clear visualization of the primary grain distribution without visual interference^[34]. From Fig.6, it is evident that the number of nucleated grains in the TiB₂-Ni₆₀Cr₂₁Fe₁₉ model surpasses that of the Ni₆₀Cr₂₁Fe₁₉ model.

Fig.7 depicts the evolution of crystal structure proportions and dislocation density over time. Commencing at approximately 0.9 ns, the proportions of FCC and HCP structures commence their ascent, stabilizing around 1.4 ns. In contrast, the proportion of BCC structures maintains a comparatively mea-

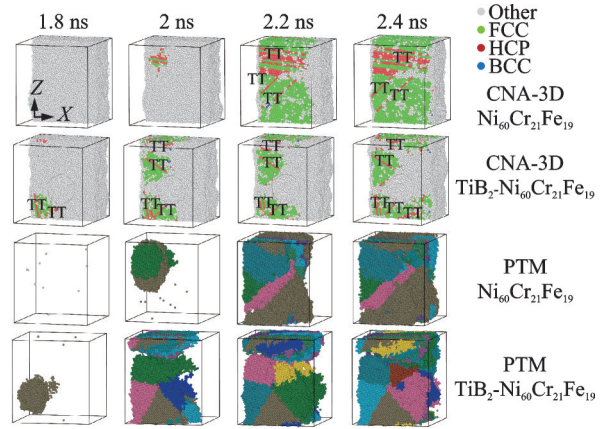


Fig.6 Crystal growth process during rapid directional solidification

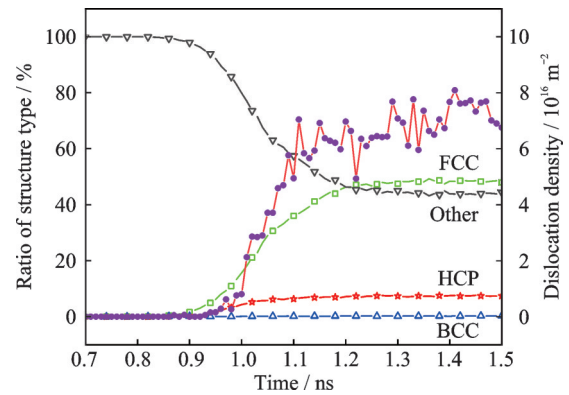


Fig.7 Variation of crystal structure and dislocation density over time during rapid directional solidification

ger presence. At 1.5 ns, the proportions of FCC, HCP, and BCC structures are 47.9%, 7.4%, and 0.3%, respectively. Notably, amorphous grain boundaries constitute a substantial portion, profoundly influencing both the microstructure and overall performance characteristics of the material. Throughout the metal rapid directional solidification process, dislocation density experiences a marked surge, culminating in a relatively stable, high-density state of approximately 10^{16} m^{-2} .

Fig.8 clearly illustrates the temporal variations in crystal structure proportions among various elemental constituents. In the initial stages of grain growth, these crystal structures exhibit relative stability. As the rapid directional solidification progresses, Ni, Cr, and Fe atoms predominantly accumulate in FCC and amorphous configurations, with a minimal presence in HCP structures. Conversely, BCC structures consistently exhibit low contents of these atoms, hovering around 1%–2%, and are

virtually absent in the amorphous phase. Notably, TiB_2 , an inorganic compound, remains in an amorphous state throughout the rapid directional solidification process due to its non-melting nature, retaining Ti and B atoms in this state. A noteworthy trend is the enrichment of Ni atoms in FCC structures, suggestive of compositional segregation within the FCC structures. This heterogeneous distribution of elements significantly influences the alloy's corrosion and oxidation resistance, pivotal considerations in additive manufacturing processes.

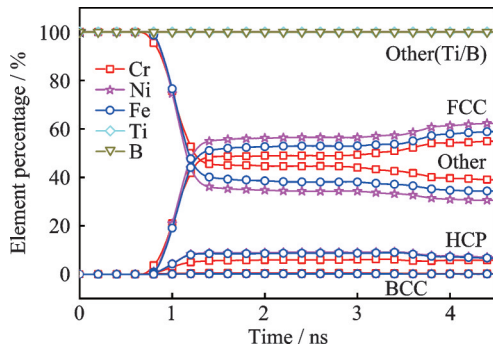


Fig.8 Evolution of elemental proportions in various crystal structures during the rapid directional solidification process

2.2 Effect of TiB_2 nanoparticles on nucleation rate

The evolution of the number of grain during the rapid directional solidification process is shown in Fig.9. According to the classical nucleation theory, the nucleation rate I_r can be expressed as^[35]

$$I_r = N_0 v \exp\left[-\frac{k_1 \sigma^3 f(\theta)}{k_B T (\Delta G_v)^2}\right] \quad (4)$$

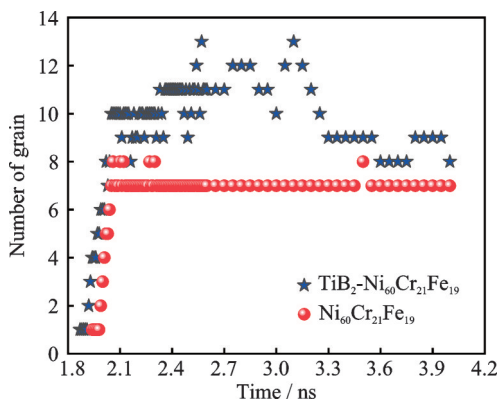


Fig.9 Evolution of number of grain during rapid directional solidification of $\text{Ni}_{60}\text{Cr}_{21}\text{Fe}_{19}$ and $\text{TiB}_2\text{-Ni}_{60}\text{Cr}_{21}\text{Fe}_{19}$

$$\Delta G_v = \frac{\Delta H \Delta T}{T_m} \quad (5)$$

where N_0 is the temperature-dependent pre-exponential factor; v the frequency related to the viscosity of atoms crossing the liquid-solid interface; k_1 the geometric factor; k_B the Boltzmann constant; T the current temperature, typically measured in Kelvin; $f(\theta)$ the catalytic activity factor between 0 and 1, depending on the value of the wetting angle θ ; ΔH the latent heat of fusion; T_m the liquidus temperature, which is the temperature at which the mixture is heated until it is completely liquefied; and ΔT the degree of undercooling. These two equations describe the relationship between the nucleation rate I_r and the undercooling ΔT . The undercooling ΔT is the difference between the theoretical crystallization temperature and the actual crystallization temperature, reflecting the extent to which the system deviates from equilibrium.

According to Eqs. (4, 5), higher undercooling leads to a higher nucleation rate. Typically, rapid cooling rates result in finer grain structures. This is attributed to the fact that under conditions of high undercooling, the nucleation rate surges, prompting the formation of an increased number of nuclei. However, the grain growth rate remains relatively subdued, curbing the expansion of each individual nucleus. Consequently, this gives rise to finer grains, which provide more potential nucleation sites. It is crucial to note that Eq.(4) exhibits a heightened sensitivity to errors in the undercooling level. Even slight deviations in undercooling level can significantly alter the predicted nucleation rate, causing discrepancies that may span several orders of magnitude from the anticipated value.

To facilitate a more straightforward determination of the nucleation rate, a simpler model is employed, as defined by

$$I_r = \frac{n}{\tau V} \quad (6)$$

where n is the number of nuclei in the simulation box, V the volume of the simulation box, which is specified as 10^3 nm^3 in this paper, and τ the induction time. The induction time is from the onset of nucleation to the formation of the final microstructure.

Based on the MD simulation results and the calculation method defined by Eq.(6), Table 1 presents the predicted values of the average nucleation rates and grain diameters for Ni₆₀Cr₂₁Fe₁₉ alloy systems with and without TiB₂ nanoparticles acting as nucleating agents during the rapid directional solidification process.

Table 1 Predicted average nucleation rate I_v and grain diameter d

Parameter	n	$\tau/$ ns	$I_v/$ ($\text{m}^{-3}\cdot\text{s}^{-1}$)	$d/$ nm
Ni ₆₀ Cr ₂₁ Fe ₁₉	7	0.565	1.27×10^{34}	8.22
TiB ₂ -Ni ₆₀ Cr ₂₁ Fe ₁₉	13	0.510	2.55×10^{34}	7.10

A pronounced effect is evident from the data; the introduction of TiB₂ nanoparticles significantly boosts the average nucleation rate of the Ni₆₀Cr₂₁Fe₁₉ alloy, escalating it from $1.27 \times 10^{34} \text{ m}^{-3}\cdot\text{s}^{-1}$ to $2.55 \times 10^{34} \text{ m}^{-3}\cdot\text{s}^{-1}$. Correspondingly, this enhancement leads to a notable reduction in the average grain diameter, aligning with the grain refinement phenomenon documented by Chen et al.^[10] in their experimental studies. TiB₂ nanoparticles, acting as heterogeneous nucleation sites during the alloy's solidification, facilitate the proliferation of nucleation events within the molten alloy. These abundant nucleation sites accelerate the nucleation process, resulting in the formation of a finer grain structure characterized by a higher density of grains. Moreover, TiB₂ nanoparticles exhibit a pronounced grain boundary pinning effect, where they stabilize at grain boundaries and hinder their free movement. This physical constraint restricts the migration of grain boundaries, effectively suppressing abnormal grain growth at elevated temperatures. Consequently, the refined grain structure is maintained, further optimizing the microstructure of the Ni₆₀Cr₂₁Fe₁₉ alloy and potentially enhancing its mechanical properties.

2.3 Anisotropic behavior of tensile performance

To comprehensively evaluate the anisotropic tensile properties of the alloy and the pivotal influence of TiB₂ nanoparticles as nucleating agents on these properties, an exhaustive study encompassing four distinct tensile simulation tests has been meticulously conducted. This rigorous investigation delves

into two fundamental microstructural variants within the Ni₆₀Cr₂₁Fe₁₉ alloy system: One incorporates TiB₂ nanoparticles as nucleating agents, emphasizing grain refinement, and the other devoid of these nanoparticles. The testing regime further encompassed two orthogonal tension directions: The X -direction, aligning with the rapid directional solidification direction, and the Z -direction, oriented perpendicular to rapid directional solidification direction.

Fig.10(a) meticulously illustrates the tensile specimen, clearly marking the cross-sectional area that is further examined in Fig.10(b). Fig.10(b) then provides a comprehensive overview of the tensile stress-strain curves under different scenarios, accompanied by precise CNA microstructural images captured from the designated cross-section as shown in Fig.10(a), specifically at points 1, 2, and 5 along the stress-strain curves. Moreover, a statistical analysis of the dislocation line lengths at points 1 through 7 has been neatly tabulated within Fig.10(b), facilitating a deeper understanding of the microstructural evolution.

Fig.10 vividly illustrates the contrasting tensile stress-strain curves of these configurations, revealing that the Ni₆₀Cr₂₁Fe₁₉ alloy with TiB₂ nanoparti-

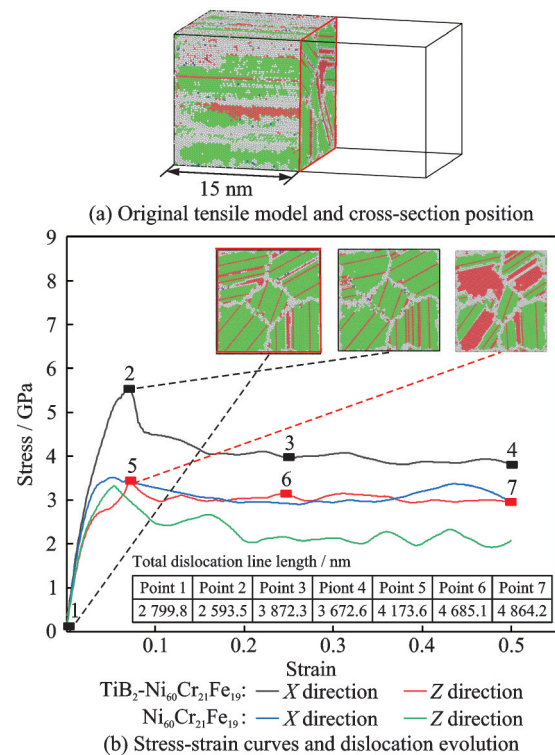


Fig.10 Tensile anisotropy of solidified microstructure

cles as nucleating agents exhibits a remarkable tensile strength of approximately 5.8 GPa along the X -direction, significantly surpassing the strength of around 3.5 GPa observed along the Z -direction. This disparity underscores the alloy's pronounced anisotropic tensile behavior.

Under X -axis tension, the analysis reveals an intriguing trend: An initial subtle reduction in dislocation line length, followed by a steady and consistent increase. This phenomenon is postulated to be intimately linked to the unique dislocation dynamics evolution mechanisms specific to this loading orientation. Conversely, under Z -axis tension, the dislocation density exhibits a relentless surge, maintaining a consistently high level. This dense dislocation network structure is hypothesized to facilitate premature plastic deformation by effectively lowering the stress threshold required to initiate deformation, thereby enhancing the alloy's deformation response.

Upon comparing the stress-strain curves under X -axis tension between the $\text{Ni}_{60}\text{Cr}_{21}\text{Fe}_{19}$ alloy with and without TiB_2 nanoparticles as nucleating agents, a pronounced enhancement in tensile strength attributable to the presence of TiB_2 nanoparticles becomes evident. This substantial boost in strength is attributed to the efficacious grain refinement facilitated by the TiB_2 nanoparticles, with the grain strengthening mechanism emerging as a pivotal factor.

2.4 Microstructure evolution during tension

By employing the CNA algorithm and the dislocation extraction algorithm (DXA)^[36], both integrated within the OVITO software platform, we conduct a thorough examination of the intricate evolution of dislocations and the transformation of microstructures within the cross-section of the tensile sample depicted in Fig.10(a) during the process of tensile loading. This detailed analysis is presented in Figs.11(a—e). Figs.11(a, c, e) show DXA images without particle information, while Figs. (b, d, f) display DXA images that contain particle information. This visualization employs a color-coded scheme to differentiate various dislocation types, enhancing clarity and interpretability. Specifically,

green dislocation lines signify Shockley dislocations, magenta lines designate Stair-rod dislocations, yellow lines represent Hirth dislocations, dark blue lines correspond to Perfect dislocations, light blue lines denote Frank dislocations, and red lines encapsulate other dislocation types that do not fall into the aforementioned classifications. This nuanced approach allows for a comprehensive understanding of the dislocation dynamics and microstructural transformations under tensile stress.

At the onset of tensile deformation along the X -direction, the dislocation landscape and twin structures exhibit a relatively ordered arrangement, accompanied by a notably high dislocation density, as evident in Figs.11(a, b). As the tensile strain ϵ gradually increases to 0.05, an intriguing yet apparent paradox arises: The direct visual count of dislocation lines seems to diminish, as depicted in Figs.11(c, d). However, this diminution is a misleading indicator of dislocation density's true nature. Instead, it stems from the intricate interplay among dislocations, where opposing directional vectors facilitate mutual cancellation or recombination. This microscale dynamic equilibrium masks the underlying robust dislocation activity, resulting in an apparent decrease in observable dislocation lines.

A significant phenomenon during this stage is the generation of a large number of intrinsic stacking faults (ISFs) and extrinsic stacking faults (ESFs). These stacking faults, as additional planar defects in the crystal structure, not only reflect the intensification of dislocation activity but also indicate changes in the internal energy state of the material.

As the strain ϵ further increases to 0.125, dislocation activity significantly intensifies. Dislocations continuously proliferate and intertwine, forming a complex dislocation network. This network greatly increases the complexity of dislocation movement, significantly enhancing the material's strength and hardness through hindrance effects. Fragmented mechanical twins (MTs) are generated during tensile loading. These fragmented twin structures do not significantly impede dislocations, leading to a smoother stress flow and a downward trend in stress levels, as shown in Figs.11(e, f).

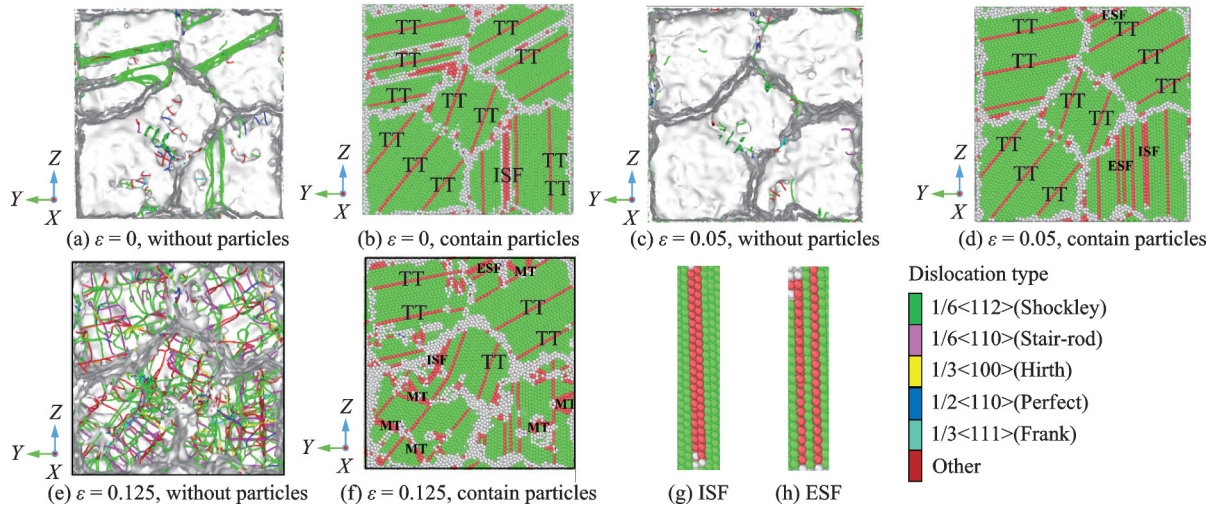


Fig.11 Microstructural evolution of the sample's cross-section during tensile testing along the rapid directional solidification direction (X -direction)

Figs.11(g, h) provide an insightful glimpse into the internal structural transformations occurring within the crystal previously shown in Fig.11(d). These images illustrate the formation of ISF induced by deviations in the stacking sequence of specific atomic layers, and the subsequent evolution of partial dislocations into ESF under the influence of the fault structures.

During the tensile test along the Z -direction, as the tensile strain reaches 0.05, the number of dislocations significantly increases, and the density of dislocation lines intensifies notably. Concurrently, more twin boundaries and a few mechanical twins form within the material, indicating a substantial change in the microstructure under loading conditions, as illustrated in Figs.12(a, b).

When the tensile strain in the Z -direction attains 0.125, the dislocation count further surges, and the distribution pattern of dislocation lines becomes more intricate, with instances of dislocation entanglement emerging. Additionally, the number of twin regions within the material grows substantially, displaying a clear trend of expansion and forming relatively flat mechanical twins, as depicted in Figs.12(c, d).

Upon comparing the microstructural evolution under tensile loading along the X -axis and Z -axis, as presented in Figs.11, 12, we can elucidate the phenomenon observed in Fig.10, wherein the tensile strength along the Z -axis is markedly inferior to

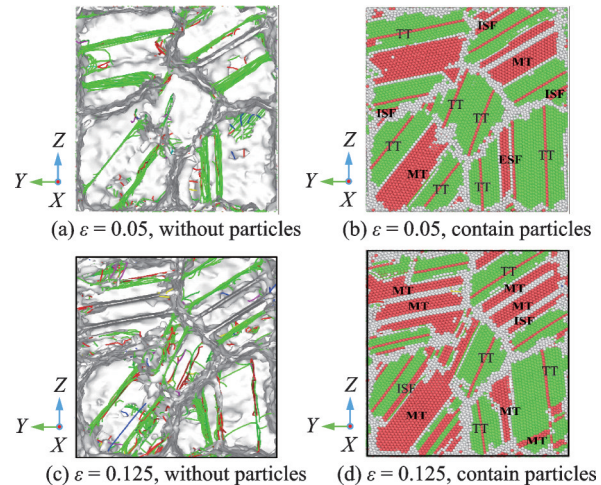


Fig.12 Microstructural evolution of the sample's cross-section during tensile testing perpendicular to the rapid directional solidification direction (Z -direction)

that along the X -axis. Notably, the Z -axis tensile process fosters the development of more pronounced and well-organized mechanical twins. These twin structures function as efficient slip planes, offering smoother avenues for dislocation motion, thereby significantly enhancing stress relaxation and distribution.

In contrast, the mechanical twins that form under X -axis tensile loading exhibit a more fragmented nature, with their morphology and distribution less favorable for dislocation slip and stress relief compared to the Z -axis orientation. Consequently, the stress-alleviating mechanisms along the X -axis are not as pronounced, resulting in a more rapid accu-

mulation of stress under identical loading conditions. This, in turn, contributes to the higher tensile strength observed in the X -axis direction.

3 Conclusions

This study employed MD simulations to investigate the effects of TiB_2 nanoparticles on the nucleation and grain growth mechanisms of IN718 alloy during rapid directional solidification, and explored the tensile anisotropy of the solidified microstructures. The key findings are:

(1) After rapid directional solidification, the MD solidification simulations of the alloy, adhering to grain growth principles from low to high temperature regions, show a microstructure dominated by FCC structures interspersed with thermally induced twins, minor HCP and BCC structures, numerous amorphous grain boundaries, and significant Ni segregation within the FCC structure of the $\text{Ni}_{60}\text{Cr}_{21}\text{Fe}_{19}$ alloy, maintaining a high dislocation density of $10^{16}/\text{m}^2$.

(2) TiB_2 nanoparticles acts as heterogeneous nucleation sites during metal rapid directional solidification, providing abundant nucleation locations that facilitated grain formation and effectively increased the nucleation rate.

(3) Incorporating TiB_2 nanoparticles into models with different loading directions reveals higher tensile strength in the X -direction compared to the Z -direction. This is attributed to smoother mechanical twins, acting as slip planes, generated during Z -axis tension, which facilitates dislocation migration, rapid stress release, and uniform stress distribution, thereby influencing the overall mechanical properties.

(4) Under the same loading direction, the addition of TiB_2 nanoparticles significantly enhanced the tensile strength along the rapid directional solidification direction.

References

- [1] LAI Jianhua, WANG Shili, LIU Jia, et al. Simulation and experimental study on electrochemical broaching of GH4169 turbine disk slot[J]. Journal of Nanjing University of Aeronautics & Astronautics, 2024, 56(1): 44-54. (in Chinese)
- [2] WANG L, LIU M Y, LIU Y, et al. Research progress on surface impact strengthening mechanisms and application of nickel-based superalloys[J]. Acta Metallurgica Sinica, 2023, 59(9): 1173-1189.
- [3] ZHU Guoliang, LUO Hua, HE Jian, et al. Advances in additive manufacturing of nickel-based high-temperature alloys[J]. Journal of Materials Engineering/Cailiao Gongcheng, 2024, 52(2): 1-15. (in Chinese)
- [4] LEE H, JUNG J E, KANG D S, et al. Oxide dispersion strengthened IN718 owing to powder reuse in selective laser melting[J]. Materials Science and Engineering: A, 2022, 832: 142369.
- [5] KLADOVASILAKIS N, CHARALAMP-OUS P, TSONGAS K, et al. Influence of selective laser melting additive manufacturing parameters in Inconel 718 superalloy[J]. Materials, 2022, 15(4): 1362.
- [6] GUAN J, WANG Q. Laser powder bed fusion of dissimilar metal materials: A review[J]. Materials, 2023, 16(7): 2757.
- [7] LIU Z, ZHAO D, WANG P, et al. Additive manufacturing of metals: Microstructure evolution and multistage control[J]. Journal of Materials Science & Technology, 2022, 100: 224-236.
- [8] SHENG J, HUANG S, ZHOU J, et al. Effects of warm laser peening on the elevated temperature tensile properties and fracture behavior of IN718 nickel-based superalloy[J]. Engineering Fracture Mechanics, 2017, 169: 99-108.
- [9] GAO Xiaolong. The selection refiner of pure nickel and on the refinement mechanism[D]. Lanzhou: Lanzhou University of Technology, 2009. (in Chinese)
- [10] CHEN Y, JIAN Z, REN Y, et al. Influence of TiB_2 volume fraction on SiCp/AlSi10Mg composites by LPBF: Microstructure, mechanical, and physical properties[J]. Journal of Materials Research and Technology, 2023, 23: 3697-3710.
- [11] SHIBUTA Y, SAKANE S, MIYOSHI E, et al. Heterogeneity in homogeneous nucleation from billion-atom molecular dynamics simulation of solidification of pure metal[J]. Nature Communications, 2017, 8(1): 10.
- [12] DENG H, WANG L, LIU Y, et al. Microstructure and tensile properties of IN-718 superalloy aged with temperature/stress coupled field[J]. Journal of Materials Research and Technology, 2023, 23: 47-56.
- [13] KUMAR S, RAO G S, CHATTOPADH-YAY K, et al. Effect of surface nanostructure on tensile behavior of superalloy IN718[J]. Materials & Design (1980—2015), 2014, 62: 76-82.

- [14] CAO Z. Directional solidification of alloys for additive manufacturing[D]. Munich: Technical University of Munich, 2021.
- [15] FUJINAGA T, WATANABE Y, SHIBUTA Y. Nucleation dynamics in Al solidification with Al-Ti refiners by molecular dynamics simulation[J]. Computational Materials Science, 2020, 182: 109763.
- [16] BAHRAMYAN M, MOUSAVIAN R T, CARTON J G, et al. Nano-scale simulation of directional solidification in TWIP stainless steels: A focus on plastic deformation mechanisms[J]. Materials Science and Engineering: A, 2021, 812: 140999.
- [17] LIU X, CHANG L, MA T, et al. Molecular dynamics simulation of tension and compression deformation behavior in CoCrCuFeNi high-entropy alloy: Effects of temperature and orientation[J]. Materials Today Communications, 2023, 36: 106523.
- [18] HU J, HAOTIAN Z, YOULIN Z, et al. Molecular dynamics simulation of tensile deformation of nanometer multilayer Cu/Ta materials[J]. Materials and Technology, 2022, 56(4): 415-422.
- [19] MENDELEV M I, BOROVIKOV V. Finnis-sinclair potential for the Fe-Ni-Cr system developed by Mendeleev et al[EB/OL]. [2024-03-15]. https://openkim.org/id/MO_922363340570_000.
- [20] ATTARIAN S, XIAO S. Development of a 2NN-MEAM potential for TiB system and studies of the temperature dependence of the nanohardness of TiB₂[J]. Computational materials science, 2022, 201: 110875.
- [21] WANG H P, ZHENG C H, ZOU P F, et al. Density determination and simulation of Inconel 718 alloy at normal and metastable liquid states[J]. Journal of Materials Science & Technology, 2018, 34(3): 436-439.
- [22] BASKES M I. Modified embedded atom potentials for cubic materials and impurities[J]. Physical Review B, 1992, 46(5): 2727.
- [23] ZHAO M Q, SONG J, TANG Q, et al. Laser powder bed fusion of Inconel 718-based composites: Effect of TiB₂ content on microstructure and mechanical performance[J]. Optics & Laser Technology, 2023, 167: 109596.
- [24] JIMBA Y, KONDO S, YU H, et al. Effect of mechanically alloyed sintering aid on sinterability of TiB₂[J]. Ceramics International, 2021, 47(15): 21660-21667.
- [25] ZHOU X W, FOSTER M E, SILLS R B. An Fe-Ni-Cr embedded atom method potential for austenitic and ferritic systems[J]. Journal of Computational Chemistry, 2018, 39(29): 2420-2431.
- [26] DONG H, FAN L, MOON K, et al. MEAM molecular dynamics study of lead free solder for electronic packaging applications[J]. Modelling and Simulation in Materials Science and Engineering, 2005, 13(8): 1279.
- [27] KURDI A, ALDOSHAN A, ALSHABOUNA F, et al. Investigation into the microstructure and hardness of additively manufactured (3D-printed) Inconel 718 Alloy[J]. Materials, 2023, 16(6): 2383.
- [28] KO W S, KIM D H, KWON Y J, et al. Atomistic simulations of pure tin based on a new modified embedded-atom method interatomic potential[J]. Metals, 2018, 8(11): 900.
- [29] ARKUNDATO A, SU'UD Z, ABDULL-AH M, et al. Molecular dynamic simulation on iron corrosion-reduction in hightemperature molten lead-bismuth eutectic[J]. Turkish Journal of Physics, 2013, 37(1): 132-144.
- [30] HIREL P. AtomsK: A tool for manipulating and converting atomic data files[J]. Computer Physics Communications, 2015, 197: 212-219.
- [31] PLIMPTON S. Fast parallel algorithms for short-range molecular dynamics[J]. Journal of computational physics, 1995, 117(1): 1-19.
- [32] STUKOWSKI A. Visualization and analysis of atomistic simulation data with OVITO—The open visualization tool[J]. Modelling and Simulation in Materials Science and Engineering, 2009, 18(1): 015012.
- [33] FAKEN D, JönSSON H. Systematic analysis of local atomic structure combined with 3D computer graphics[J]. Computational Materials Science, 1994, 2(2): 279-286.
- [34] LARSEN P M, SCHMIDT S, SCHIØT-Z J. Robust structural identification via polyhedral template matching[J]. Modelling and Simulation in Materials Science and Engineering, 2016, 24(5): 055007.
- [35] MAHATA A, ZAEEM M A, BASKES M I. Understanding homogeneous nucleation in solidification of aluminum by molecular dynamics simulations[J]. Modelling and Simulation in Materials Science and Engineering, 2018, 26(2): 025007.
- [36] WANG Y, SHI J. Texture control of Inconel 718 superalloy in laser additive manufacturing by an external magnetic field[J]. Journal of Materials Science, 2019, 54: 9809-9823.

Acknowledgements This work was supported by the National Natural Science Foundation of China (Nos.12462006,

12062016); the high-performance computing services offered by the Information Center of Nanchang Hangkong University.

Authors Mr. WANG Jin received the B.E. degree in mechanical design, manufacturing and automation from College of Science and Technology, Nanchang Hangkong University (NCHU), in 2022. His research is focused on numerical simulation in laser additive manufacturing.

Prof. JIANG Wugui received the B.E., M.S. and Ph.D. degrees in engineering mechanics from Nanchang University (NCU), Nanchang, China, in 1997, 2000 and 2003, respectively. He is currently a professor in School of Aeronautical Manufacturing Engineering at NCHU. He is also a distinguished member of the Jinggang Scholars Program, a prestigious accolade in Jiangxi Province. With international experience as a Visiting Scholar at Nanyang Technological University, Singapore, City University of Hong Kong, China,

Australian National University and Queensland University of Technology, Australia, he has established valuable networks and contributed to the advancement of his research field on a global scale. His recent interest lies in multiscale modeling for advanced manufacturing mechanics, and laser additive manufacturing.

Author contributions Mr. WANG Jin constructed the model, conducted data analysis, interpreted the results, and wrote the manuscript. Prof. JIANG Wugui provided guidance for the modeling ideas of this model, analysis of images, and writing of the paper. Mr. HU Chenxi contributed to the discussion and background sections of the research. All authors commented on the manuscript draft and approved the submission.

Competing interests The authors declare no competing interests.

(Production Editor: SUN Jing)

TiB₂纳米颗粒对Ni₆₀Cr₂₁Fe₁₉合金快速定向凝固过程微观组织和力学性能的影响:分子动力学研究

王 津, 江五贵, 胡晨曦

(南昌航空大学材料科学与工程学院, 南昌 330063, 中国)

摘要:采用分子动力学(Molecular dynamics, MD)方法,探讨了TiB₂纳米颗粒在Inconel 718高温合金快速定向凝固过程中对晶粒细化、微观结构演化以及拉伸性能的影响,重点研究了TiB₂纳米颗粒在Ni₆₀Cr₂₁Fe₁₉合金体系快速定向凝固过程中如何有效提升形核率。为进一步评估凝固后微观结构的拉伸性能及其各向异性行为,本文进行了后续的拉伸模拟。MD模拟结果显示,在Ni₆₀Cr₂₁Fe₁₉合金的快速定向凝固过程中加入TiB₂纳米颗粒后,平均形核率从 $1.27 \times 10^{34} \text{ m}^{-3} \cdot \text{s}^{-1}$ 跃升至 $2.55 \times 10^{34} \text{ m}^{-3} \cdot \text{s}^{-1}$ 。此外,在面心立方(Face centered cube, FCC)结构中,Ni原子呈现出明显的成分偏析现象,且凝固后的合金具有极高的位错密度,达到了 10^{16} m^{-2} 。研究还发现,快速定向凝固过程导致微观结构呈现出明显的各向异性特征。具体表现为,沿凝固方向的拉伸强度明显优于垂直于凝固方向的拉伸强度。这种差异主要源于不同加载方向下变形机制的不同。在垂直于凝固方向的拉伸应力作用下,形成了平滑且有序的机械孪晶,这些孪晶作为滑移面,有效增强了位错迁移率,从而改善了应力的松弛和分散。此外,研究结果还进一步验证了TiB₂纳米颗粒在细晶强化方面的显著效果,特别是在提高沿快速定向凝固方向的拉伸强度方面表现突出。

关键词: TiB₂纳米颗粒;快速定向凝固;微观组织演变;分子动力学